

MECHANICAL PROPERTIES OF ZR-BASED BULK METALLIC GLASS PARTS FABRICATED BY LASER-FOIL-PRINTING ADDITIVE MANUFACTURING

Yingqi Li, Ming C. Leu, and Hai-Lung Tsai

Department of Mechanical and Aerospace Engineering, Missouri University of Science and Technology, Rolla,
MO 65409

Abstract

The application of bulk metallic glasses (BMGs) has been traditionally limited to parts with small dimensions and simple geometries, due to the requirement of fast cooling during the conventional process of casting. This research exemplifies a promising additive manufacturing method, i.e., laser-foil-printing (LFP), to fabricate high-quality BMG parts with large dimensions and complex geometries. In this study, $Zr_{52.5}Ti_5Al_{10}Ni_{14.6}Cu_{17.9}$ BMG parts were fabricated by LFP technology in which MG foils are laser welded layer-by-layer upon a substrate. The mechanical properties of the fabricated BMG parts were measured using micro-indentation, tensile test and four-point bending test, and then compared to as-cast BMG parts. Through LFP, as rapid cooling rates can be achieved, fully amorphous and nearly fully dense BMG parts without cracking have been successfully made. The fabricated BMG parts exhibit mechanical properties, including micro-hardness, tensile strength, and flexural strength, comparable with the as-cast BMG parts.

Keywords: Metallic glass, Laser processing, Additive manufacturing, Mechanical properties

Introduction

Metallic glasses (MGs), also known as amorphous alloys, are solid metallic materials with amorphous atomic structures [1]. MG can be formed if a molten metal is cooled down fast enough to avoid crystallization. Owing to the amorphous atomic structure and concomitant lack of grain boundaries or dislocations which are the “weak regions” of crystalline metals, MGs usually exhibit many exceptional properties, such as high strength (even an ultrahigh strength of over 5 GPa), hardness, elasticity, corrosion resistance, wear resistance, etc., compared to conventional crystalline metals [1,2].

The first MG, with a chemical composition of $Au_{75}Si_{25}$, was synthesized in 1960 by Duwez’s group at Caltech [3]. Because metal atoms crystallize so rapidly, they developed rapid quenching techniques to cool the liquid metal down at very high rates of 10^5 – 10^6 K/s. Since then, a large number of studies on the conventional MGs fabricated by rapid quenching techniques, e.g., melt spinning method, have been carried out [4]. However, because of the required high cooling rate to obtain amorphous structure, conventional MGs could only be tens or hundreds of microns thick, which is too thin for most practical applications.

The thickness limitation was drastically reduced by the findings of bulk metallic glass (BMG) alloy compositions. BMGs are typically multicomponent alloys designed near deep eutectics which require much lower critical cooling rates (as low as ~ 0.1 K/s) to suppress crystallization during solidification [4]. Many kinds of BMG alloy compositions have been developed including Pd-based, Zr-based, Ti-based, Ni-based, Cu-based, Mg-based, Fe-based, etc. [5,6]. The dramatic decrease in the critical cooling rate has enabled the production of thicker MG parts, and a change in the production method from rapid quenching to copper mold casting. The critical plate thickness, which is defined as the largest plate thickness of glass formation achieved by copper mold casting, has reached > 10 mm for BMG systems based on Zr, Pd, Pt, Mg, La, Ni and Cu, and > 5 mm for BMG systems based on Fe, Co and Ti [7,8].

Although the critical cooling rates for glass formation have been significantly reduced, the thickness of as-cast BMG parts does not “proportionally” increase. For example, the critical cooling rate of $Zr_{52.5}Ti_5Al_{10}Ni_{14.6}Cu_{17.9}$ BMG, which is selected for this study, is ~ 10 K/s, but its critical plate thickness is only around 4 mm [8]. As heat at the internal locations of an ingot must be transferred by conduction to the outer surface and then dissipates to the surroundings, the center of an ingot has the lowest cooling rate. As long as the critical cooling rate can be achieved at the center of an ingot, the entire sample will be amorphous. The cooling rates inside the metal are controlled by its thermophysical properties (e.g., thermal conductivity). Generally, BMGs have lower melting temperatures and thermal conductivities than those of the major individual elements of the alloys [9]. For example, Zr-based BMGs have very low thermal conductivity (~ 7 W/m·K) as compared to that of the major elements in the alloy, e.g., Zr (~ 23 W/m·K). Heat cannot be rapidly conducted to the outer surface and then dissipated to the surrounding cooling medium, especially when the part has a large cross-section area. This greatly limits the fabrication of large-size BMG parts by casting. In addition, only a limited range of geometries can be fabricated through direct casting of BMGs, since ideal molding conditions demand slow filling of mold cavity, which is problematic when fast cooling is required for glass formation [2]. To exploit the potential of BMGs, there is a necessity to explore new processing techniques for the fabrication of complicated BMG parts with larger dimensions.

Laser-based additive manufacturing (AM) technology is a promising method to overcome the size and geometry limitations of BMG products imposed by casting. As a layer-by-layer manufacturing technology, AM has an intrinsic advantage of fabricating 3D parts with intricate geometries [10]. In addition, the requirement of high cooling rates can be decoupled from the part dimensions in AM as it fragments the “casting” process of a part into many small volumes [11]. Theoretically, as long as high cooling rates can be fulfilled in each layer, BMG parts of any dimension can be made. On the other hand, the heating and cooling rates of laser processing are usually very high (10^4 – 10^5 K/s), which highly facilitates the formation of amorphous layer and could even allow the processing of BMGs with weak glass-forming ability.

A number of studies have been conducted using laser-based AM to fabricate BMG parts [11–24]. Most of these studies were conducted through selective laser melting (SLM) in which MG powder was used as feedstock and parts were made through melting the powder in a bed. SLM has yielded fully amorphous BMG parts from Zr-based or Ti-based MG powder with strong glass-forming ability [11,12,14]. However, when using powder as feedstock, challenges exist to achieve BMG parts that are dense, crack-free and fully amorphous at the same time as explained below. First, the powder bed density is not very high, leading to as much as 40–50% free space [25]. One consequence of this free space is that the powder bed has much lower thermal conductivity than the bulk material. For example, the measured thermal conductivity of a 316L stainless steel powder bed is only about 0.3–5% of that of the bulk material [26]. Such low thermal conductivity is problematic for the processing of BMG which requires the heat to be removed rapidly. Hence, to suppress crystallization, small laser energy input is required. On the other hand, the gas present in the powder bed will significantly increase the possibility of forming pores. To fully melt powder and reduce porosity, higher laser energy input is usually desired. However, it might cause crystallization of BMG, especially in the heat-affected zone (HAZ). Once crystallization occurs, cracks are easily formed since crystallized BMGs are usually brittle.

Metal foil is another kind of feedstock material that can be used for AM. For AM of BMG parts, metal foil has obvious advantages over metal powder. First, metal foils have much better thermal contact than powders and thus higher thermal conductivity. Heating and cooling rates when using foil should be higher than those when using powder at the same or similar laser processing conditions. Second, foil has no pores/gaps inside, and therefore less effort is needed to reduce porosity. Hence, when using foil as feedstock, crystallization of BMG is less likely to occur while parts with high densities can be achieved.

In this study, we utilize MG foil with a nominal composition of $Zr_{52.5}Ti_5Al_{10}Ni_{14.6}Cu_{17.9}$ as feedstock to fabricate BMG parts using a newly developed AM technology, called laser-foil-printing (LFP). We have demonstrated the capability of LFP technology to fabricate dense, crack-free and fully amorphous Zr-based BMG

parts with 3D geometries and thicknesses exceeding the critical plate thickness in previous publications [20,22]. This paper focuses on the mechanical properties of BMG parts fabricated by LFP, and compares them to as-cast parts, in order to demonstrate the potential of LFP for achieving high-quality BMG parts.

Experimental

The LFP process was used in this study. More details explaining the LFP process and the system developed for this technology at Missouri S&T can be found in our other publication [27]. To facilitate discussion below, a short description is given here. The LFP system mainly consists of two lasers: a continuous wave fiber laser with 1070 nm wavelength for foil-welding and a pulsed UV laser with 355 nm wavelength and 30 ns pulse duration for foil-cutting. In the process of fabricating each layer, a metal foil is fixed upon a flat substrate by laser spot-welding, and then a laser raster-scan welding process is done to achieve the full fusion and bonding of foil in selected regions. After the laser welding is done, the workpiece is translated to the location under the UV laser beam. Then, the UV laser cuts the welded foil along the contour of the sliced cross section of the 3D part to be fabricated. After the laser cutting is completed, the foil left is removed and a fresh foil is placed on the top of the workpiece for fabricating the next layer. This procedure is repeated until the desired 3D part is completely built. The process is performed inside a chamber with Ar shielding gas.

In this study, $Zr_{52.5}Cu_{17.9}Ni_{14.6}Al_{10}Ti_5$ (at.%) MG foil was used as the feedstock (see Fig. 1(a)). The MG foil was commercial grade alloy and was manufactured through slow melt spinning (produced by Liquidmetal Technologies, Inc.). Each layer of foil is 200 μm thick. Before the LFP process, the foil was slightly polished using 240 grit SiC paper followed by ethanol cleaning in order to remove possible surface oxides. Rectangular BMG parts were then fabricated by LFP on a Ti-6Al-4V substrate. To achieve a good bonding between the BMG part and the Ti substrate, two layers of pure Zr foil (200 μm thick for each layer) were firstly welded onto the substrate as the intermediate layers, as shown in Fig. 1(b). After that, MG foils were welded layer-by-layer onto the workpiece to fabricate a BMG part (Fig. 1(c)). More discussion on the dissimilar metals bonding between the BMG part and the Ti substrate can be found in our previous publication [22].

For the welding of MG foil, the laser power ($P = 500$ W), the hatch space between two laser scanning passes ($\Delta d = 0.15$ mm), and the beam diameter ($d = 170$ μm) were kept constant. Crystallization of BMG during laser processing is related to laser energy input. In this experiment, two laser scanning speeds (v) were used, i.e., $v = 350$ mm/s and 500 mm/s, to achieve a high energy input and a relatively low energy input. The above parameters were selected after parametric studies to ensure continuous, stable and sound welding passes.

After the BMG parts were built, they were cut from the substrates using wire electrical discharge machining (EDM) for characterization. For comparison, as-cast BMG parts with the same chemical composition were also characterized. The as-cast parts were also commercial grade alloy and were fabricated by injection molding (also produced by Liquidmetal Technologies, Inc.). It should be noted that except tensile test all other characterizations in the following were performed on as-cast beams that were 3.5 mm thick, 3.8 mm wide, and 60 mm long (see Fig. 1(d)).

X-ray diffraction (XRD, Philips X'pert MPD) was used to characterize the formed phases. Optical microscopy (Nikon Epiphot 200) was performed on the cross-section of the LFP samples to analyze the microstructure and possible defects. The metallographic specimens for optical microscope analysis were first grinded using 240 grit and 600 grit SiC papers, and then polished using 9 μm and 3 μm diamond suspensions. This was followed by a final polishing with the application of 0.04 μm colloidal silica suspension.

The micro-hardness was measured using a Vickers micro-hardness tester (Struers, Duramin 5) with 500 g load and 10 s load duration. The tensile strength of the LFP part along the laser scan direction was tested. The dimensions of the tensile specimen can be found in [22], with a thickness of around 0.8 mm. The tensile specimens for the as-cast part were cut from a 0.75-mm-thick plate. 50-mm-long beams with 3 mm square cross-section were cut from the LFP part and the as-cast part using wire EDM for four-point bending test. The tension side of the four-point bending beam was grinded to a final 600 grit surface finish, while other sides were grinded to a

120 grit surface finish. The tensile and four-point bending tests were conducted on an INSTRON universal testing machine. The speed of the machine crosshead was maintained at 0.015 mm/mm/min for tensile test and 0.50 mm/min for four-point bending test. The tensile strain was measured by a clip-on extensometer, while the bending displacement was measured by the crosshead. The load span and the support span for the four-point bending test were 20 mm and 40 mm, respectively. All the samples were bent in the thickness direction. Three specimens were tested for each group, and the average value with one standard deviation was reported.

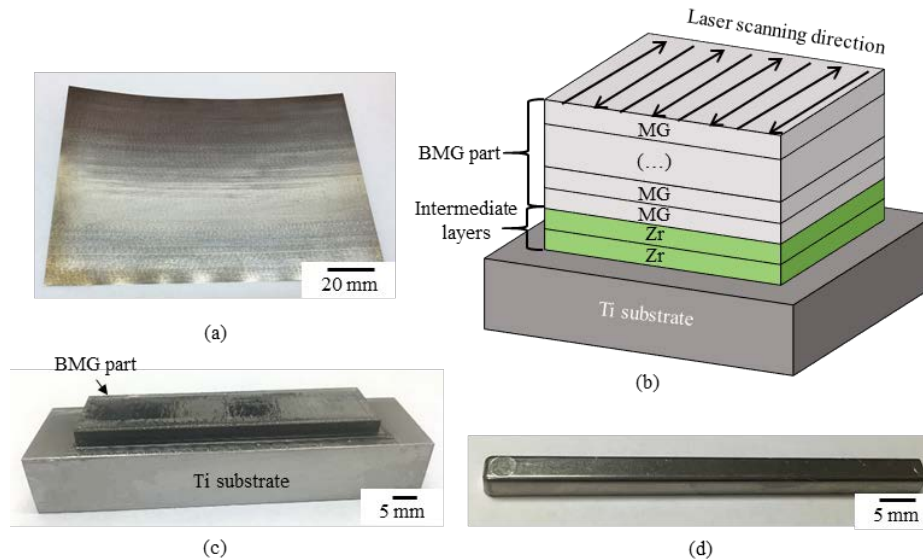


Figure 1 (a) MG foil used as the feedstock for LFP; (b) schematic of a LFP part building process; (c) a BMG part fabricated on a Ti substrate; (d) as-cast BMG beam.

Results and Discussion

The XRD patterns of the cast sample, the foil feedstock, and the LFP samples are shown in Fig. 2. The XRD pattern of the cast sample was obtained on the cross-section perpendicular to the length direction. For the LFP samples, the XRD analysis was conducted on the cross-section perpendicular to the laser scanning direction. The irradiation area of the X-ray beam was larger than $2 \times 2 \text{ mm}^2$. Hence, the XRD result in Fig. 2 is a representative of the entire sample. It can be seen that the XRD patterns of the foil feedstock, the cast sample and the LFP sample with low energy input all only show the characteristic broad peak from the amorphous structure, indicating that they are fully amorphous within the detection limit of XRD ($\sim 2\%$) [28]. For the LFP sample with high energy input, its X-ray pattern shows the broad peak from the amorphous structure as well as several sharp Bragg peaks from crystalline phases, indicating that this sample is partially crystallized. Since there are five elements (Zr, Al, Ni, Cu, and Ti) involved and too few Bragg peaks detected, it is difficult to identify the possible crystalline phases present in this sample. The formed crystalline phases may be NiZr_2 , CuTi_3 , AlZr_2 , Al_3Ti , etc.

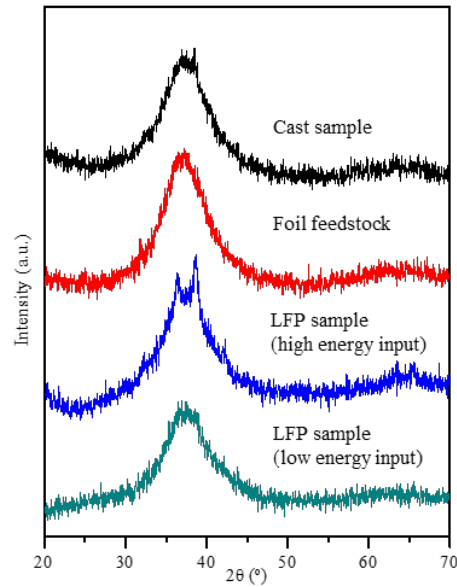


Figure 2 XRD patterns of the foil feedstock, cast sample, and LFP samples.

Figures 3(a) and 3(b) are the optical micrographs of the cross-sections from the bottom to the top surface of the LFP samples with high energy input and with low energy input, respectively. The cross-sections of different locations were inspected by optical microscope, and Figs. 3(a) and 3(b) just show the representative optical micrographs. For the LFP sample with high energy input, visible pores were not observed from its cross-sections, while the cross-sections of the LFP sample with low energy input have few pores, as shown in Fig. 3(b). ImageJ software was then used to measure the porosity through calculating the area fraction of pores on the optical micrographs (same magnification as Fig. 3(b)) of several cross-sections with a total area of $\sim 10 \times 3.5 \text{ mm}^2$. The measured porosity of the LFP with low energy input is only $\sim 0.1\%$.

In addition, cracking is not observed from the cross-sections of both LFP samples, although partial crystallization occurred in the LFP sample with high energy input (see Fig. 2). Figure 3(c) is the optical micrograph of the weld surface of the LFP sample showing the overlapped laser scanning passes. It can be seen that the weld surface of the LFP sample is smooth. The cross-sections of the LFP samples were then etched using a solution of 100 ml H_2O , 2 ml H_2O_2 and 0.1 ml HF to reveal their microstructures. For the LFP sample with low energy input, its optical micrograph of the cross-section after etching, which is not shown here because it is similar to Fig. 3(b), is featureless since this sample is fully amorphous, which is consistent with the XRD result (see Fig. 2). For the LFP sample with high energy input, its optical micrographs of the cross-section after etching are shown in Figs. 3(d) and 3(e). Small crystals (appear dark) are observed in the LFP sample with high energy input, which disperse throughout the amorphous matrix (appears bright). The size of the crystals is around $7 \mu\text{m}$. Using ImageJ, the area fraction of crystals for Figs. 3(d) and 3(e) is calculated to be $\sim 4\%$.

Micro-hardness, tensile and four-point bending tests were then conducted to evaluate the mechanical properties of the LFP samples. The micro-hardness values of the cast sample and the LFP samples are listed in Table 1. The reported micro-hardness value is an average of ten measurements with one standard deviation. The micro-hardness value of the cast sample averages to 549 HV. The LFP sample with low energy input, which is fully amorphous, has nearly the same micro-hardness value as the cast sample. For the LFP sample with high energy input, which is partially crystallized, its micro-hardness value is around 579 HV, which is slightly higher than those of the cast sample and the LFP with low energy input. The increased micro-hardness of the LFP sample with high energy input is caused by the formation of crystals in the amorphous matrix. The formed crystalline phases are intermetallic compounds (see Fig. 2) which are usually harder than the amorphous phase [22].

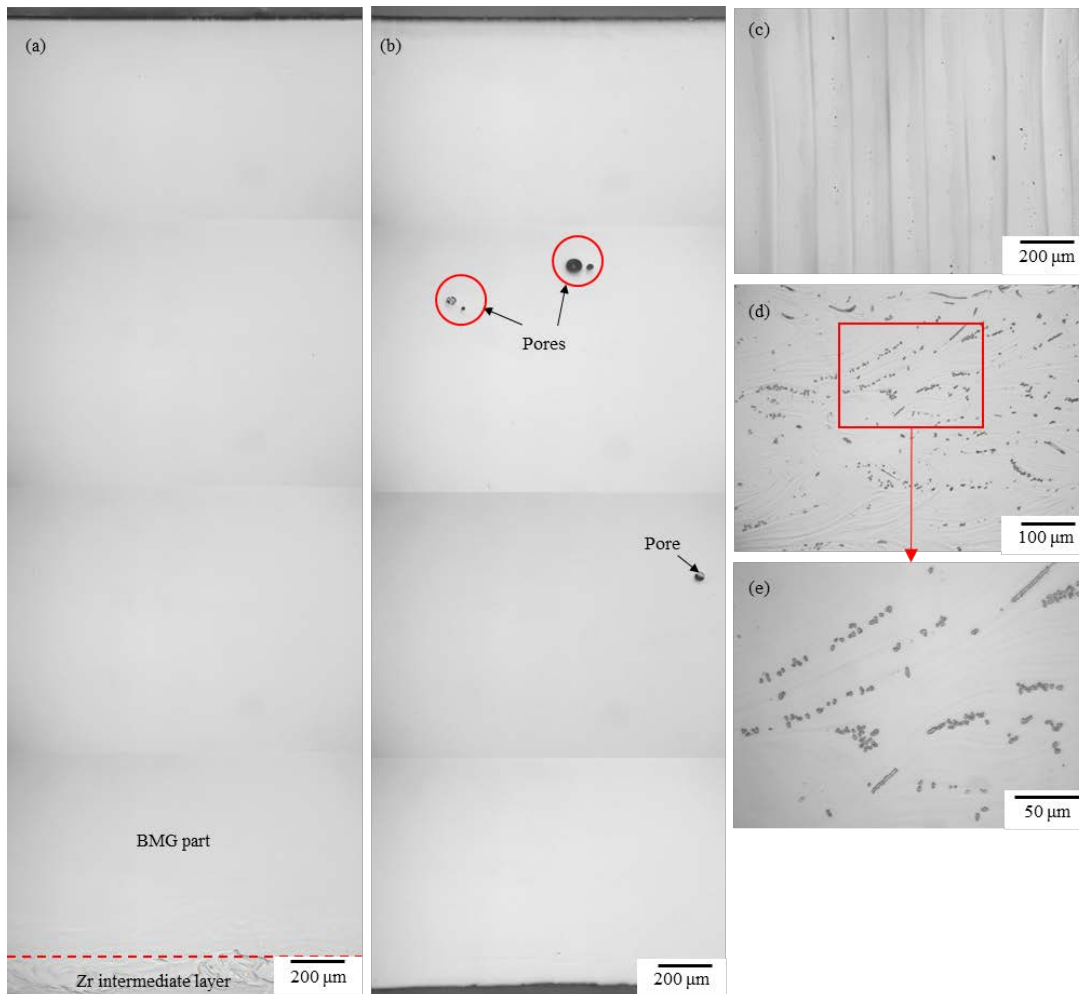


Figure 3 Optical micrographs of the LFP samples: (a) cross-section of the sample with high energy input; (b) cross-section of the sample with low energy input; (c) top surface showing the overlapped scanning passes; (d) and (e) magnified cross-section views of the sample with high energy input after etching showing the formed crystalline phases (dark) dispersing in the amorphous matrix (bright).

Table 1 Micro-hardness, ultimate tensile strength, and maximum flexural strength of the cast sample and LFP samples.

Sample	Cast sample	LFP sample (high energy input)	LFP sample (low energy input)
Micro-hardness (HV)	549 ± 11	579 ± 11	551 ± 18
Ultimate tensile strength (MPa)	1791 ± 30	1856 ± 17	1796 ± 60
Maximum flexural strength (MPa)	2096 ± 212	2096 ± 108	2186 ± 109

Figure 4(a) shows the representative tensile stress–strain curves of the cast sample and the LFP samples. The ultimate tensile strength (UTS) with one standard deviation values are summarized in Table 1. It can be seen that the LFP sample with low energy input exhibits nearly the same UTS as the cast sample, which is 1791 ± 30 MPa. Similar to the micro-hardness results, the UTS of the LFP sample with high energy input, which is 1856 ± 17 MPa, is also slightly higher than those of the cast sample and the LFP sample with low energy input. This

might be caused by the strengthening effect of the crystalline phases [29]. In addition, all the samples nearly show zero tensile ductility and exhibit catastrophic fracture. The total tensile strain prior to fracture is about 1.2%.

The optical micrographs in Fig. 5 show that the tensile specimens of the cast sample and the LFP samples all fractured in a shear mode. The formation and propagation of one major shear band dominated the fracture process during tensile test. The lack of tensile ductility of BMG is caused by the free and rapid propagation of the shear band since there are no microstructure or other stabilizing features to arrest the slipping shear band [30]. As shown in Figs. 5(a), 5(c) and 5(e), the tensile fracture angle between the tensile axis and the fracture plane is measured around 55° for all samples. This fracture angle deviates from the angle of the maximum shear stress plane which is 45° . It might be caused by the effect of normal tension stress acting on the fracture plane that can promote the shear fracture of BMGs, and the larger fracture angle corresponds to a higher normal tension stress [31]. The SEM micrographs of the fracture surfaces are shown in Figs. 5(b), 5(d) and 5(f). It can be seen that the fracture surfaces are relatively smooth and they all exhibit a vein pattern which is the characteristic tensile or compression fracture morphology of BMGs. The vein pattern was attributed to temperature rise and subsequent local melting within the shear band induced by the high elastic energy in instantaneous fracture [31,32]. Due to the melting of MG within the shear band, the molten MG easily flows and appears in a vein pattern.

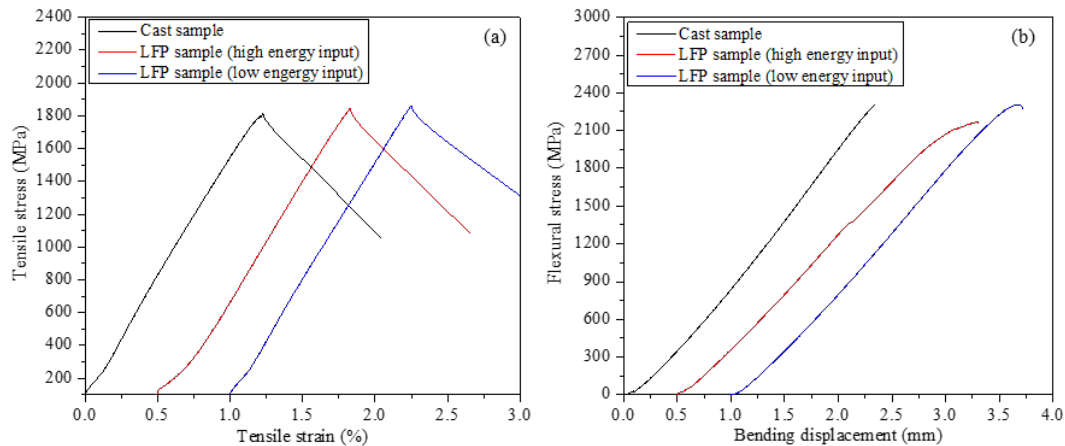


Figure 4 (a) Tensile stress–strain curves and (b) flexural stress–bending displacement curves of the cast sample and LFP samples.

In addition to tensile strength, flexural strength was also measured through four-point bending test. The maximum flexural strength values of the cast sample and the LFP samples are summarized in Table 1. Figure 4(b) shows the typical flexural stress–bending displacement curves of the cast sample and the LFP samples. We can see that the LFP sample with high energy input has the same maximum flexural strength as the cast sample, which is averaged to 2096 MPa. Unlike the tensile test results in which the LFP sample with high energy input demonstrates the highest UTS, the maximum flexural strength of the LFP sample with low energy input is the highest one and its average value is 2187 MPa. For all samples, the beams show limited plastic deformation prior to failure (see Fig. 4(b)). From the above mechanical testing results, we can see that the LFP samples exhibit nearly the same mechanical properties as the cast sample. Even in the presence of a small amount of crystals ($\sim 4\%$), the LFP sample with high energy input still displays comparable or even higher strength in bending and tensile test than the cast sample, indicating that a small amount of crystals embedded in the amorphous matrix would not deteriorate the mechanical properties of the BMG parts. However, if the volume fraction of crystalline phases in the BMG part is too high, the part will become very brittle [11,29].

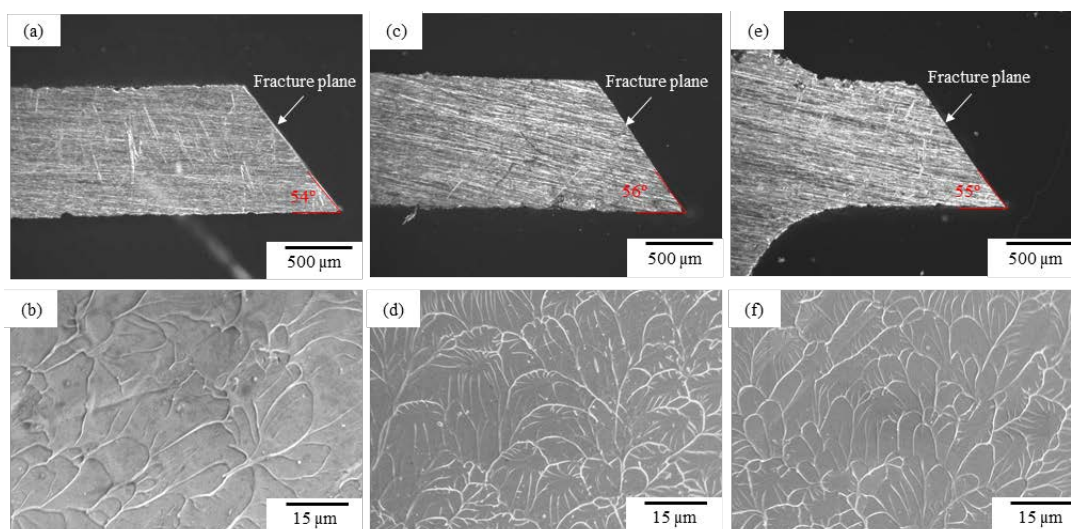


Figure 5 Optical micrographs (the first row) showing the shear fracture and SEM images showing the fracture surfaces (the second row) of the tensile specimens: (a) and (b) cast sample; (c) and (d) LFP sample with high energy input; (e) and (f) LFP sample with low energy input.

Conclusions

Zr_{52.5}Cu_{17.9}Ni_{14.6}Al₁₀Ti₅ bulk metallic glass (BMG) parts were fabricated by laser-foil-printing (LFP) additive manufacturing. The mechanical properties of the LFP parts were measured and compared to parts made by conventional casting. The results show that LFP is able to produce fully amorphous BMG parts with nearly full density (~ 99.9%). In addition, the LFP sample with fully amorphous has a micro-hardness of 551 ± 18 HV, an ultimate tensile strength of 1796 ± 60 MPa, and a maximum flexural strength of 2186 ± 109 MPa, while the cast sample has a micro-hardness of 549 ± 11 HV, an ultimate tensile strength of 1791 ± 30 MPa, and a maximum flexural strength of 2096 ± 212 MPa. Even in the presence of a small amount of crystals (~ 4%), the partially crystallized LFP part still displays comparable or even higher strength in bending and tensile test than the cast part. This study demonstrates that LFP has the potential for fabricating high-quality BMG parts with mechanical properties comparable to cast parts. The properties of the LFP parts can be further optimized if the quality (purity, contamination, etc.) of the foil feedstock and the manufacturing technology (shielding chamber, cooling media, etc.) are improved.

Acknowledgement

This work was supported by the Department of Energy [grant number DE-FE0012272] and the University of Missouri System [award number FastTrack-16002R].

References

- [1] W.H. Wang, C. Dong, C.H. Shek, Bulk metallic glasses, *Mater. Sci. Eng. R*, 44 (2004) 45-89.
- [2] J. Schroers, Processing of bulk metallic glass, *Adv. Mater.*, 22 (2010) 1566-1597.
- [3] W.K. Jun, R. Willens, P. Duwez, Non-crystalline structure in solidified gold-silicon alloys, *Nature*, 187 (1960) 869.
- [4] M. Chen, A brief overview of bulk metallic glasses, *NPG Asia Materials*, 3 (2011) 82-90.
- [5] A. Inoue, F.L. Kong, S.L. Zhu, E. Shalaan, F.M. Al-Marzouki, Production methods and properties of engineering glassy alloys and composites, *Intermetallics*, 58 (2015) 20-30.
- [6] A. Inoue, A. Takeuchi, Recent progress in bulk glassy, nanoquasicrystalline and nanocrystalline alloys, *Mater. Sci. Eng. A*, 375-377 (2004) 16-30.
- [7] A. Inoue, A. Takeuchi, Recent development and application products of bulk glassy alloys, *Acta Mater.*, 59 (2011) 2243-2267.

- [8] J. Na, G. Garrett, K. Han, G. Kaltenboeck, C. Crewdson, M.D. Demetriou, W.L. Johnson Zirconium-titanium-copper-nickel-aluminum glasses with high glass forming ability and high thermal stability, US20170241006A1, US, 2017.
- [9] M. Yamasaki, S. Kagao, Y. Kawamura, K. Yoshimura, Thermal diffusivity and conductivity of supercooled liquid in Zr₄₁Ti₁₄Cu₁₂Ni₁₀Be₂₃ metallic glass, *Appl. Phys. Lett.*, 84 (2004) 4653.
- [10] Y. Huang, M.C. Leu, J. Mazumder, A. Donmez, Additive Manufacturing: Current State, Future Potential, Gaps and Needs, and Recommendations, *ASME J. Manuf. Sci. Eng.*, 137 (2014) 014001.
- [11] S. Pauly, C. Schricker, S. Scudino, L. Deng, U. Kühn, Processing a glass-forming Zr-based alloy by selective laser melting, *Mater. Des.*, 135 (2017) 133-141.
- [12] L. Deng, S. Wang, P. Wang, U. Kühn, S. Pauly, Selective laser melting of a Ti-based bulk metallic glass, *Mater. Lett.*, 212 (2018) 346-349.
- [13] H.Y. Jung, S.J. Choi, K.G. Prashanth, M. Stoica, S. Scudino, S. Yi, U. Kuhn, D.H. Kim, K.B. Kim, J. Eckert, Fabrication of Fe-based bulk metallic glass by selective laser melting: A parameter study, *Mater. Des.*, 86 (2015) 703-708.
- [14] X.P. Li, M.P. Roberts, S. O'Keeffe, T.B. Sercombe, Selective laser melting of Zr-based bulk metallic glasses: Processing, microstructure and mechanical properties, *Mater. Des.*, 112 (2016) 217-226.
- [15] Z. Mahbooba, L. Thorsson, M. Unosson, P. Skoglund, H. West, T. Horn, C. Rock, E. Vogli, O. Harrysson, Additive manufacturing of an iron-based bulk metallic glass larger than the critical casting thickness, *Appl. Mater. Today*, 11 (2018) 264-269.
- [16] D. Ouyang, N. Li, L. Liu, Structural heterogeneity in 3D printed Zr-based bulk metallic glass by selective laser melting, *J. Alloy. Compd.*, 740 (2018) 603-609.
- [17] D. Ouyang, N. Li, W. Xing, J. Zhang, L. Liu, 3D printing of crack-free high strength Zr-based bulk metallic glass composite by selective laser melting, *Intermetallics*, 90 (2017) 128-134.
- [18] S. Pauly, L. Löber, R. Petters, M. Stoica, S. Scudino, U. Kühn, J. Eckert, Processing metallic glasses by selective laser melting, *Mater. Today*, 16 (2013) 37-41.
- [19] C. Yang, C. Zhang, W. Xing, L. Liu, 3D printing of Zr-based bulk metallic glasses with complex geometries and enhanced catalytic properties, *Intermetallics*, 94 (2018) 22-28.
- [20] Y. Shen, Y. Li, C. Chen, H.L. Tsai, 3D printing of large, complex metallic glass structures, *Mater. Des.*, 117 (2017) 213-222.
- [21] P. Bordeenithikasem, Y. Shen, H.L. Tsai, D.C. Hofmann, Enhanced mechanical properties of additively manufactured bulk metallic glasses produced through laser foil printing from continuous sheetmetal feedstock, *Additive Manufacturing*, 19 (2018) 95-103.
- [22] Y. Li, Y. Shen, M. C. Leu, H.L. Tsai, Building Zr-based Metallic Glass Part on Ti-6Al-4V Substrate by Laser-Foil-Printing Additive Manufacturing, *Acta Mater.*, 144 (2018) 810-821.
- [23] Y. Li, Y. Shen, C.H. Hung, M.C. Leu, H.L. Tsai, Additive manufacturing of Zr-based metallic glass structures on 304 stainless steel substrates via V/Ti/Zr intermediate layers, *Mater. Sci. Eng. A*, 729 (2018) 185-195.
- [24] Y. Li, Y. Shen, C. Chen, M.C. Leu, H.L. Tsai, Building metallic glass structures on crystalline metal substrates by laser-foil-printing additive manufacturing, *J. Mater. Process. Technol.*, 248 (2017) 249-261.
- [25] T.G. Spears, S.A. Gold, In-process sensing in selective laser melting (SLM) additive manufacturing, *Integrating Materials and Manufacturing Innovation*, 5 (2016).
- [26] L.C. Wei, L.E. Ehrlich, M.J. Powell-Palm, C. Montgomery, J. Beuth, J.A. Malen, Thermal conductivity of metal powders for powder bed additive manufacturing, *Additive Manufacturing*, 21 (2018) 201-208.
- [27] C. Chen, Y. Shen, H.L. Tsai, A Foil-Based Additive Manufacturing Technology for Metal Parts, *ASME J. Manuf. Sci. Eng.*, 139 (2016) 024501.
- [28] B.A. Sarsfield, M. Davidovich, S. Desikan, M. Fakes, S. Futernik, J.L. Hilden, J.S. Tan, S. Yin, G. Young, B. Vakkalagadda, K. Volk, Powder X-ray diffraction detection of crystalline phase in amorphous pharmaceuticals, *International Centre for Diffraction Data* (2006) 322-327.
- [29] J. Eckert, J. Das, S. Pauly, C. Duhamel, Mechanical properties of bulk metallic glasses and composites, *J. Mater. Res.*, 22 (2011) 285-301.
- [30] J. Qiao, H. Jia, P.K. Liaw, Metallic glass matrix composites, *Mater. Sci. Eng. R*, 100 (2016) 1-69.

- [31] Z.F. Zhang, J. Eckert, L. Schultz, Difference in compressive and tensile fracture mechanisms of Zr₅₉Cu₂₀Al₁₀Ni₈Ti₃ bulk metallic glass, *Acta Mater.*, 51 (2003) 1167-1179.
- [32] M. Chen, Mechanical Behavior of Metallic Glasses: Microscopic Understanding of Strength and Ductility, *Annu. Rev. Mater. Res.*, 38 (2008) 445-469.